RSC Advances

PAPER

View Article Online
View Journal | View Issue

Cite this: *RSC Adv.*, 2022, **12**, 29338

Second-phase-induced fluorescence quenching in non-equivalent substituted red phosphors†

Jun Chen,[a] Xianfeng Yang,[c] Chunyan Jiang,[a] Yunfeng Wang,*[ab] Lei Zhou *[a] and Mingmei Wu *[a]

Concentration quenching, which generally originates from serious energy migrations among the uniformly distributed luminescent centers in the host matrix, is a key factor to influence the luminescence properties of materials. Different from previous reports, we demonstrate a novel fluorescence-quenching mechanism attributable to the second-phase $Eu_2W_2O_9$ in non-equivalent substituted $SrWO_4$:xEu^{3+} phosphors. The crystal structure, elemental distribution, and luminescence properties of the as-prepared $SrWO_4$:xEu^{3+} phosphors are systematically investigated. A second-phase $Eu_2W_2O_9$ is confirmed when the Eu^{3+}-doping concentration exceeds 20%, which produces the new structure defects and energy-transfer paths, resulting in fluorescence quenching in this material. This finding gives a new perspective to analyze the concentration-quenching mechanism of the non-equivalent substituted phosphors and can help in the design of new, efficient luminescence materials. In addition, the as-prepared $SrWO_4$:xEu^{3+} phosphors exhibit a strong intrinsic excitation in the range of 355–425 nm, which is accompanied by the Commission Internationale de l'Eclairage (CIE) coordinates at (0.653, 0.347) and stable color purity of up to 94.52%. A packaged white light-emitting diode with CIE chromaticity coordinates of (0.398, 0.335), correlated color temperature of 3132 K, and color rendering index of 84.3 is fabricated by $SrWO_4$:20% Eu^{3+} phosphors with blue BAM:Eu^{2+} and green YAGB:Tb^{3+} phosphors in a near-ultraviolet chip.

Received 7th September 2022
Accepted 30th September 2022

DOI: 10.1039/d2ra05647j

rsc.li/rsc-advances

Introduction

In recent years, solid-state lighting based on inorganic luminescent materials has attracted considerable attention due to its wide range of application fields, such as lighting, display, plant growth, solar-cell utilization, optical communication, photocatalysis, and biosensors.[1–9] It is well known that concentration quenching is a common phenomenon that influences the luminescence property of doping ions. Investigations on fluorescence concentration quenching have mostly focused on equivalent and matching size substitution, such as K_2SiF_6:Mn^{4+}, $Y_3Al_5O_{12}$:Ce^{3+}, Y_2O_3:Eu^{3+}, YVO_4:Dy^{3+}, $NaYF_4$:Yb^{3+}, Er^{3+}, Y_2SiO_5:Eu^{3+}, Bi^{3+}, $BaAl_{12}O_{19}$:Eu^{2+}, and CaZnOS:Mn^{2+}.[10–17] In these reports, fluorescence activators can homogeneously disperse into the interior host lattice by replacing the equivalent ions that have similar ionic radii. According to the theoretical perspectives of Blasse, non-radiative energy can migrate among the excited emitters and reach the quenching center, which is unfavorable to luminescence.[18] Generally, a higher doping concentration can generate a much closer distance between the dopants and accelerate energy migrations. Therefore, the traditional concentration-quenching phenomenon is often observed in inorganic luminescent materials when the doping concentration exceeds a certain value.

In addition, various studies related to non-equivalent substitution have been proposed with excellent luminous performance in rare-earth- and transition-metal-ion-doped inorganic optical materials such as K_3AlF_6:Mn^{4+}, K_3ScF_6:Mn^{4+}, ZrO_2:Eu^{3+}, TiO_2:Sm^{3+}, Zn_2SiO_4:Eu^{3+}, $MMoO_4$:Eu^{3+} (M = Ca, Sr, Ba), $(CaMg)_x(NaSc)_{1-x}Si_2O_6$:$Eu^{2+}$, and $NaYF_4$:Yb^{3+}, Er^{3+}, Mn^{2+}.[19–27] Based on these reports, the luminescence centers in the non-equivalent substituted inorganic materials can produce a higher luminous efficiency owing to the perfect size matching to the replaced ions, accomplishing similar electronic densities and coordination numbers.[28] Nevertheless, the concomitant charge imbalance from non-equivalent substitution can induce some intrinsic microstructure defects such as traps, which may considerably deteriorate the luminescence performance of the as-prepared phosphor materials.[29] Some research groups have attempted to use the charge compensation method to cover the shortage and enhance the photoluminescence.[30–32] Further, many published articles on non-equivalent substituted

[a]*School of Chemistry/School of Marine Science/School of Chemical Engineering and Technology, Sun Yat-Sen University, Guangzhou 510275/Zhuhai 519082, P. R. China. E-mail: wangyunfeng@nyist.edu.cn; zhoul8@mail.sysu.edu.cn; ceswmm@mail.sysu.edu.cn*

[b]*School of Information Engineering, Nanyang Institute of Technology, Nanyang 473004, P. R. China*

[c]*Analytical and Testing Center, South China University of Technology, Guangzhou, 510640, P. R. China*

† Electronic supplementary information (ESI) available. See DOI: https://doi.org/10.1039/d2ra05647j

fluorescent materials often do not represent structure defects owing to the relatively low emitter doping concentrations.[33–35] Moreover, many studies on phosphors have pointed out the fact that non-equivalent foreign-ion doping can alter the local structure symmetry of the primary host lattice and result in an obvious phase-structure change.[36–39] Consequently, whether such a possibility exists for the typical luminescent property of the non-equivalent substituted samples mainly depends on the subsistent phase separation. To the best of our knowledge, this kind of work has not been thoroughly studied in previous literature yet.

Here, we chose the familiar $SrWO_4$:Eu^{3+} phosphors as our research object. Many experiments have confirmed that $SrWO_4$ is an excellent luminescence host due to the perfect matching size of Sr^{2+} (1.26 Å) and Eu^{3+} (1.07 Å),[40] high thermal and mechanical stability, simple route of synthesis, *etc.*[30] Therefore, scheelite-based tungsten structure hosts have attracted widespread attention and interest for use in white light-emitting diodes (WLEDs). Based on an extensive study of the concentration-quenching mechanism, the non-equivalent substituted Eu^{3+}-doped $SrWO_4$ red phosphors were prepared by a facile sol–gel method. The crystal structure, elemental distribution, and photoluminescence properties with different Eu^{3+}-doping concentrations are comprehensively studied. Accordingly, a novel concentration-quenching mechanism using phase separation has been proposed in non-equivalent substituted luminescence materials. This may provide a new perspective to investigate the inorganic luminescent materials with emitters of inconsistent charges.

Experimental section

Sample preparation

All the chemicals are of the analytical grade and used as received without further purification. Europium nitrate [$Eu(NO_3)_3 \cdot 6H_2O$] is purchased from the National Engineering Research Centre of Rare Earth Metallurgy and Function Materials. Strontium nitrate, ammonium metatungstate, and citric acid are received from Aladdin.

$SrWO_4$:xEu^{3+} phosphors were synthesized by a simple, mild sol–gel method. First, strontium nitrate, ammonium metatungstate, and europium nitrate with the corresponding stoichiometric ratio (the total number of Sr^{2+} and Eu^{3+} ions were 3 mmol) were dissolved in a mixture solution of deionized water and ethanol at a volume ratio of 1 : 1 (5 ml); 100 mg citric acid was added as the complexant. After stirring for several minutes, the homogeneous transparent solution was transferred into an oven at 70 °C to remove the deionized water and ethanol. Finally, annealing was carried out at an elevated temperature rate (180 °C h^{-1}) up to a certain high temperature within 500–1200 °C and maintained for 3 h. As a comparison, $Eu_2W_2O_9$ was prepared by the same method as described above.

Sample characterization

The phase structures of the samples were characterized by an X-ray diffractometer (XRD) using a Rigaku D-Max 2200 XRD system with Cu Kα radiation at 40 kV and 26 mA ($\lambda = 1.5405$ Å). The high-resolution transmission electron microscopy (HR-TEM) images, elemental mapping, and energy-dispersive X-ray spectroscopy (EDX) data of the samples were recorded on a JEOL JEM 2100F TEM instrument with an acceleration voltage of 200 kV. The morphology and rough elemental composition were analyzed on an FEI Quanta scanning electron microscopy (SEM) instrument equipped with an energy-dispersive spectrometer (EDS). The Raman spectra were characterized by a Horiba Jobin Yvon HR800 Raman spectrometer. The excitation source was a 488 nm laser and the diameter of the laser spot was 1.0 μm. The photoluminescence (PL) emission spectra, photoluminescence excitation (PLE) spectra, and decay curves were measured by an FLS 980-combined time-resolved and steady-state fluorescence spectrometer (Edinburgh Instruments) equipped with Xe/nF/μF lamps. Temperature-dependent PL spectra and dynamics were measured on the same instrument within a temperature range of 77–500 K. The quantum yield (QY) was obtained with a Hamamatsu C9920-03G absolute QY measurement system.

Results and discussion

Crystal structure and elemental distribution of $SrWO_4$:Eu^{3+}

The lattice structure, morphology, and elemental distribution of the $SrWO_4$:xEu^{3+} samples prepared by the simple sol–gel technique are analyzed by XRD, TEM, and SEM. The XRD patterns of the as-prepared $SrWO_4$:xEu^{3+} phosphors at an annealing temperature of 900 °C with different Eu^{3+}-doping concentrations are shown in Fig. 1a. Evidently, the samples exhibit a pure phase structure and the detected diffraction peaks match well with the International Centre for Diffraction Data (ICDD) card no. 08-0490 when the Eu^{3+} concentration varies from 2% to 20%, which seemingly indicates that the Eu^{3+} ions can homogeneously incorporate into the $SrWO_4$ host. However, when the

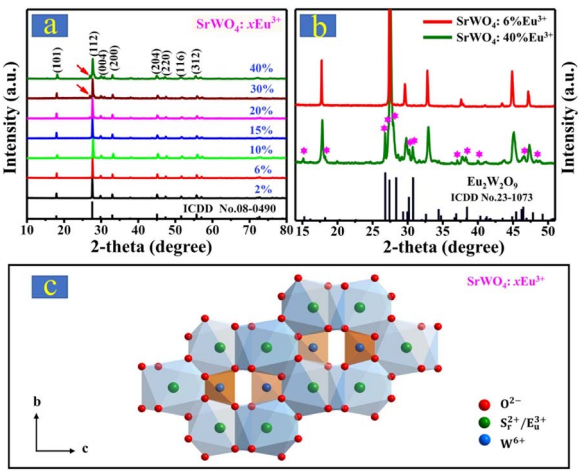

Fig. 1 (a) XRD patterns of $SrWO_4$:xEu^{3+} with different Eu^{3+} doping concentrations. (b) Comparative XRD patterns of $SrWO_4$:6%Eu^{3+} and $SrWO_4$:40%Eu^{3+}; the regular hexagon marks indicate obvious diffraction peaks of $Eu_2W_2O_9$. (c) Unit-cell representation of $SrWO_4$:Eu^{3+}.

increasing Eu^{3+} concentration is above 20%, the XRD patterns appear to have obvious impure diffraction peaks, which are ascribed to a second-phase $Eu_2W_2O_9$ distributing in the $SrWO_4$:Eu^{3+} main part with ICDD card no. 23-1073.

The comparison of the diffraction peaks of $SrWO_4$:40%Eu^{3+} and $SrWO_4$:6%Eu^{3+} (Fig. 1b) and pure $Eu_2W_2O_9$ (Fig. S1†) can definitively confirm the second phase in the as-prepared non-equivalent substituted materials. It can be deduced that some Eu^{3+} ions are not integrated into the $SrWO_4$ host lattice and combine with W^{6+} and O^{2-} groups to generate a new $Eu_2W_2O_9$ phase structure, which is derived from the existing charge balance and radius difference between Eu^{3+} and Sr^{2+} ions with a gradually increasing Eu^{3+} concentration. Different from traditional uniform Eu^{3+}-ion doping into the lattice matrix, the $Eu_2W_2O_9$ second-phase separation could be a major role to influence the photoluminescence properties in a non-equivalent substituted optical material. In addition, it can be easily observed (Fig. S2†) that the diffraction peaks gradually shift to a larger angle from 2% to 40%, which is due to the ionic radius of the replaced Sr^{2+} ($r = 1.26$ Å, CN = 8), larger than Eu^{3+} ($r = 1.07$ Å, CN = 8) emitters; this also implies that some of the Eu^{3+} ions can be evenly doped into the $SrWO_4$ host lattice. In order to better understand the crystal structure and coordination environment, a schematic of tetragonal $SrWO_4$:xEu^{3+} with the $I4_1/a$ space group is modelled (Fig. 1c). Regarding the crystallographic structure, the $SrWO_4$ host has a common tetragonal structure with the space group of $I4_1/a$ and the point-group symmetry of C_{4h}^6. The lattice parameters and unit-cell volumes of $SrWO_4$ have been calculated as $a = b = 0.542$ nm, $c = 1.196$ nm, and $V = 0.351$ nm^3, with four $SrWO_4$ formula units per tetragonal cell. In this type of structure, Sr^{2+} and W^{6+} ions are coordinated by eight and four oxygen atoms in the form of dodecahedra and tetrahedra, respectively, and the site symmetry of Sr^{2+}, W^{6+}, and O^{2-} ions is S_4, T_d, and C_1,

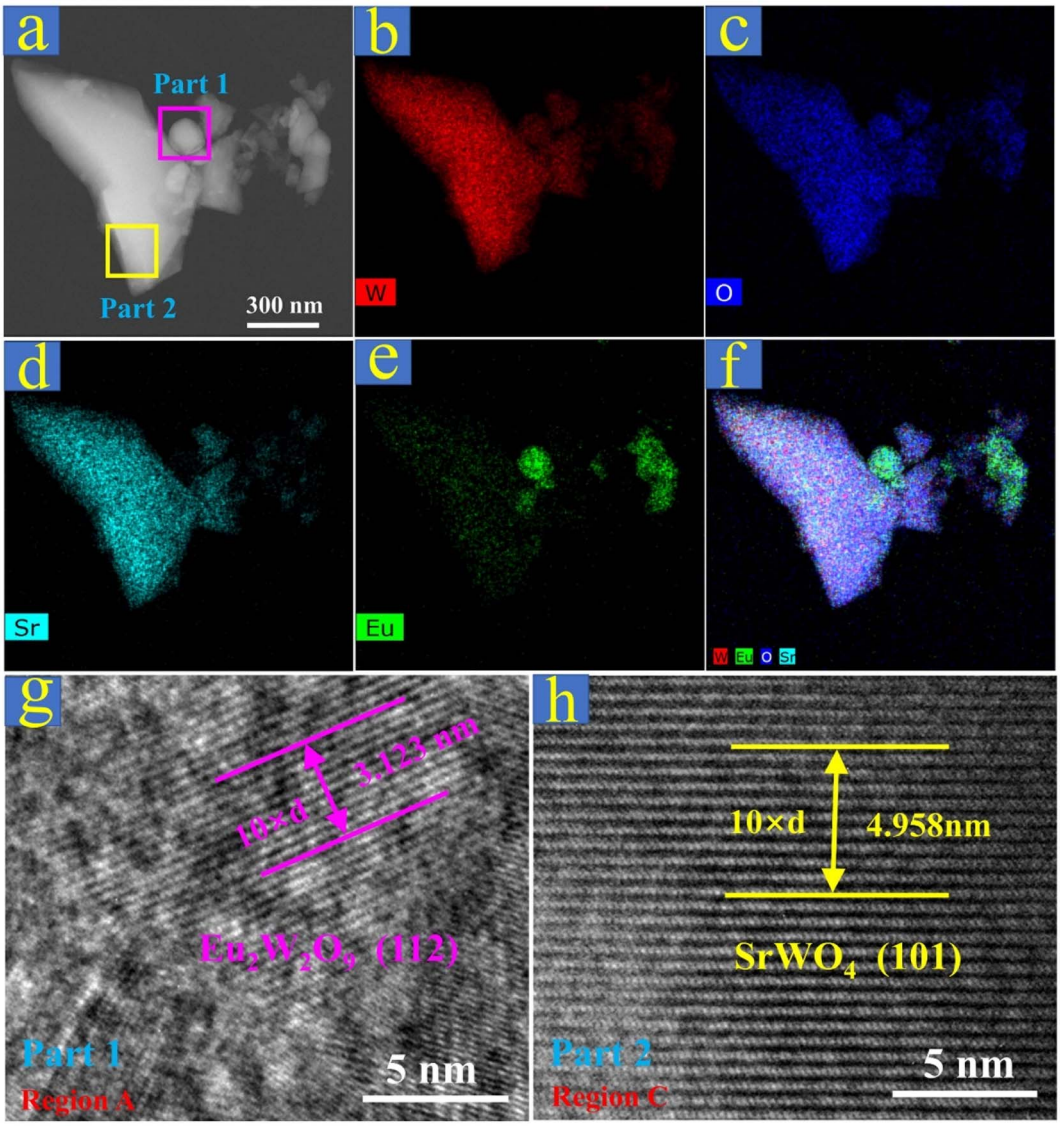

Fig. 2 (a)–(f) Scanning TEM and elemental mapping images of the as-prepared $SrWO_4$:20%Eu^{3+} sample. (g) Magnified TEM image of region A in part 1. (h) Magnified TEM image of region C in part 2.

respectively. In the unit cell of $SrWO_4$:xEu^{3+}, Eu^{3+} and Sr^{2+} ions are coordinated to eight oxygen ions and they form a distorted dodecahedron; W^{6+} ions are surrounded by four oxygen ions and constitute a slightly distorted tetrahedron.[41]

To better understand the $Eu_2W_2O_9$ second-phase separation, elemental mapping with EDX and HR-TEM images of $SrWO_4$:20%Eu^{3+} were specifically checked. In Fig. 2a, one microparticle with areas of different shapes was selected, and its elemental composition of Sr, W, Eu, and O was preliminarily detected by using the EDX spectrum (Fig. S3†). From Fig. 2b–d, it is evident that W, O, and Sr are uniformly distributed throughout the as-prepared material. However, in Fig. 2e and f, some parts are apparently rich with Eu^{3+} ions, which suggests the possible second-phase $Eu_2W_2O_9$ existing in $SrWO_4$:20%Eu^{3+} phosphors beyond the range of the XRD detection limit. The phase structure of $Eu_2W_2O_9$ can be confirmed by the HR-TEM images (Fig. 2g and S4†). The measurement result (Fig. 2g) reveals the presence of monoclinic crystalline $Eu_2W_2O_9$ possessing lattice fringes of 0.3123 and 0.2613 nm, which correspond to the (112) and (032) (Fig. S4†) crystallographic planes, respectively. Furthermore, the HR-TEM images shown in Fig. 2h and S5† exhibit the typically tetragonal crystalline $SrWO_4$ host lattice with a fringe of 0.4958 nm, which corresponds to the crystallographic plane of (101). In addition, the elementary composition and EDS by SEM images reveal that the atomic ratios of Eu, Sr, W, and O are 3.08, 13.81, 16.96, and 66.14, respectively (Fig. S6†), which is consistent with the predetermined $SrWO_4$:20%Eu^{3+}. According to the above analysis, the second-phase $Eu_2W_2O_9$ is confirmed in the non-equivalent substituted $SrWO_4$:xEu^{3+} phosphors as the Eu^{3+} concentration increases, which may have a great impact on the luminescence behavior and properties of this material.

Concentration-dependent luminescence and dynamics properties

It is well known that Eu^{3+} has the most popular red emission property because of its representative ^5D_J–^7F_J transitions.[42] The typical PLE and PL spectra of $SrWO_4$:xEu^{3+} phosphors are measured and shown (Fig. 3a) and the main population of Eu^{3+} ions at the lower-energy levels is shown in Fig. 3c for a better understanding of the PLE and PL processes of $SrWO_4$:xEu^{3+}. In the left-hand side of Fig. 3a, the PLE spectra of $SrWO_4$:xEu^{3+} are collected by monitoring the intense emission intensities at 612 nm ($^5D_0$–$^7F_2$) with different Eu^{3+}-doping concentrations from 2% to 40%. Some strong PLE peaks are located at 360, 380, 394, 413, and 463 nm, which are assigned to the transitions of $^7F_0$–$^5D_4$, $^7F_0$–^5G_J/$^5L_7$, $^7F_0$–$^5L_6$, $^7F_0$–$^5D_3$, and $^7F_0$–$^5D_2$, respectively.[33] This can provide a worthwhile advantage for producing efficient luminescence under near-UV LED chip excitation. Moreover, the diffuse reflection spectra of pure $SrWO_4$ host and $SrWO_4$:20%Eu^{3+} are recorded (Fig. S7†). An obvious absorption band of 200–350 nm is attributed to the typical energy transfer band (CTB), and some

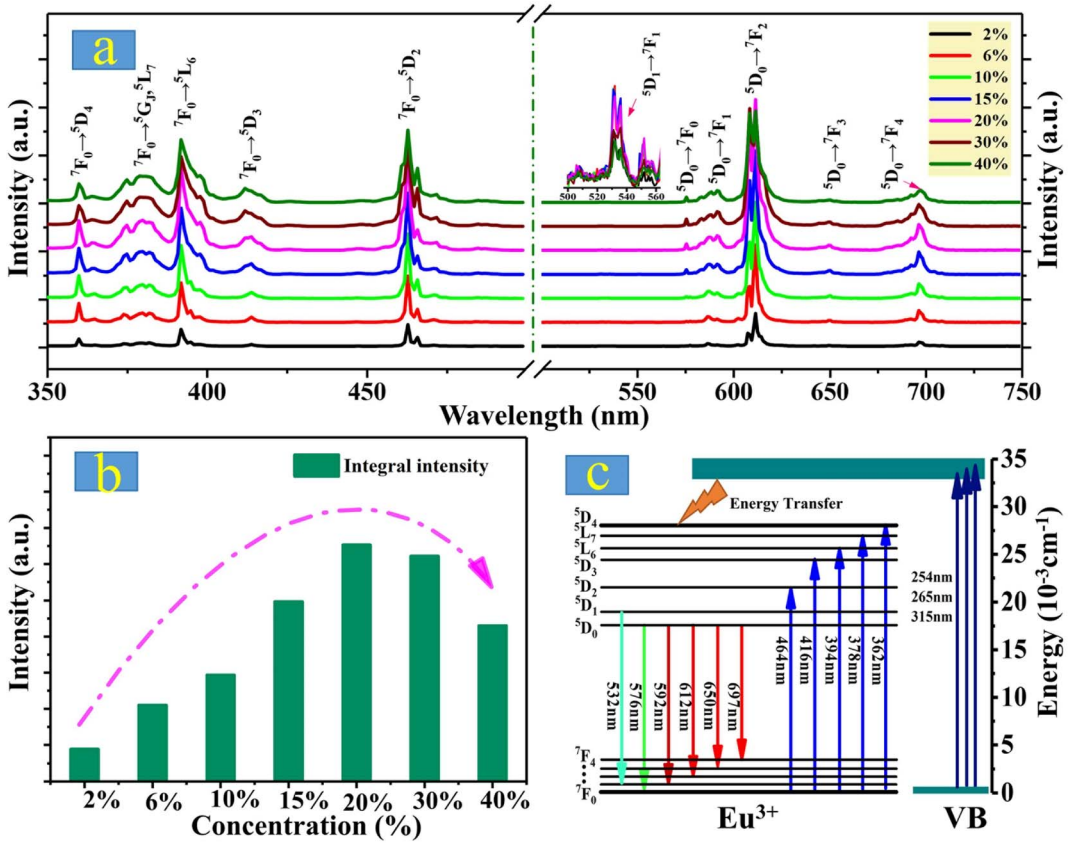

Fig. 3 (a) Concentration-dependent PLE (λ_{em} = 612 nm) and PL (λ_{ex} = 394 nm) spectra of $SrWO_4$:xEu^{3+}. (b) Histogram of the overall PL (λ_{ex} = 394 nm) intensity of $SrWO_4$:xEu^{3+}. (c) Energy-level diagram of $SrWO_4$:Eu^{3+} and possible PL processes under different excitation wavelengths.

sharp absorption peaks in the longer-wavelength region of 350–650 nm show the intrinsic absorption sites of Eu^{3+} ions from the $^7F_0$ ground state to the rich excited states.[43] These characteristics are consistent with the PLE spectra shown in Fig. 3a.

In general, the luminescent properties of materials strongly depend on the doping concentration of the activators. The right-hand side of Fig. 3a shows the typical emission lines of $SrWO_4$:xEu^{3+} (x = 2%, 6%, 10%, 15%, 20%, 30%, and 40%) under the optimal 394 nm excitation. Evidently, all the emission peaks are almost entirely covered by $^5D_0$–^7F_J transitions, which is due to the serious non-radiative relaxations of $^5D_1$–$^5D_0$ in tungstate host lattices with a large phonon threshold of 921 cm^{-1} (Fig. S8†).

Because of the very low intensity of $^5D_1$–^7F_J transitions, the color purity on red emissions of $SrWO_4$:xEu^{3+} is expected to be further optimized and marginally changed. Regarding the calculated results shown in Fig. 4, the color purity of $SrWO_4$:xEu^{3+} reaches up to 94.52% and the float does not exceed 1.1% with different Eu^{3+} concentrations (Fig. 4a).[43] The Commission Internationale de l'Eclairage (CIE) coordinates of $SrWO_4$:20% Eu^{3+} are (0.653, 0.357), which are close to the standard red emission of (0.670, 0.330), as shown in Fig. 4b. To systematically investigate the concentration-dependent PL emission properties further, Fig. 3b shows the variation tendency of the $SrWO_4$:xEu^{3+} phosphors on integral PL intensities. According to the experimental results, the integral intensities show an upward tendency before the Eu^{3+}-doping concentration reaches its optimal ratio of 20% and then gradually decreases with an increasing Eu^{3+} concentration. This common change in regularity has been reported in many rare-earth-ion-doped inorganic luminescent materials.[42] With the traditional views, Eu^{3+} ions can uniformly distribute into the $SrWO_4$ host lattices; the higher Eu^{3+}-doping concentration produces a much closer distance between the Eu^{3+} emitters and accelerates the energy migration among them. Therefore, an increasing amount of excitation energy migrates to the quenching sites and results in luminescence quenching.

However, another fluorescence-quenching path could be highlighted in the non-equivalent substituted $SrWO_4$:xEu^{3+} materials. Based on the XRD patterns and elemental distribution analyses, not all Eu^{3+} dopants can be coordinated into the $SrWO_4$ host with the increasing doping concentration as well as an increasingly serious charge imbalance. The excessive Eu^{3+} ions can combine with W^{6+} and O^{2-} groups to generate the second-phase $Eu_2W_2O_9$, which produces the new local structure defects and energy-transfer paths. Further, the excitation energy can migrate to $Eu_2W_2O_9$ or transmit inside it easily with an increasing Eu^{3+}-doping concentration. This establishes a novel concentration-quenching mechanism in rare-earth-ion-doped non-equivalent substituted materials, and the schematic of the energy-transfer relationship in $SrWO_4$:xEu^{3+} phosphors is shown in Fig. 5. Regarding the traditional concentration-quenching mechanism, the distance between the luminescence emitters is closer as the doping concentration increases, which accelerates the energy migration to make an increasing amount of energy transform into the quenching sites. Developed from the traditional concentration-quenching mechanism, a novel mechanism is proposed in which a higher doping concentration not only reduces the distance between the luminescent ions but also produces the second phase that acts as the quenching site to deteriorate the luminescence performance. Therefore, as the x values of $SrWO_4$:xEu^{3+} increases, the high Eu^{3+}-doping concentration decreases the distance of Eu^{3+} ions, on one hand, to accelerate the energy transfer between them; on the other hand, second-phase $Eu_2W_2O_9$ is generated as a special quenching site, which causes significant fluorescence quenching in this non-equivalent substituted phosphor. Further, it should be noted that under the same excitation wavelength of 394 nm, the integral emission intensity of $SrWO_4$:20%Eu^{3+} is 51% higher than that of $Eu_2W_2O_9$ (Fig. S9†), showing excellent luminescence performance. To better understand the quenching mechanism, the relation between the doping concentration and emission intensity is calculated (Fig. S10†). The experimental results can be linearly fitted with a slope of −1.58, demonstrating the dominant dipole–dipole interaction in the concentration-quenching mechanism of $SrWO_4$:xEu^{3+} phosphors.[43] We consider the internal QY η, which is defined as the ratio of the emitted to the absorbed photon number, as another reliable parameter to reflect the applicability of luminescence centers for lighting application. The QY values of $SrWO_4$:xEu^{3+} are measured under 394 nm excitation (Fig. 6). The measurement results show that the QY of the optimal sample is up to 61% with 20% Eu^{3+}-doping concentration, which is consistent with the best emission intensity.

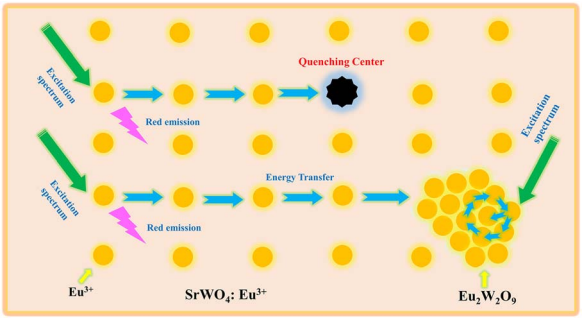

Fig. 5 Schematic of the energy-transfer relationship in $SrWO_4$:xEu^{3+} phosphors.

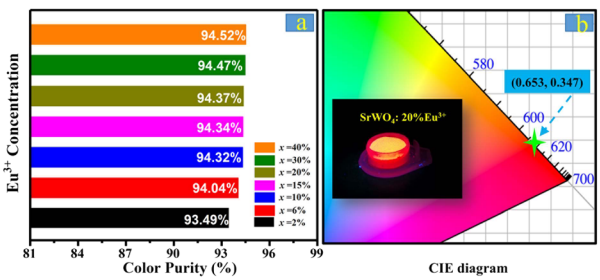

Fig. 4 (a) Color purity of $SrWO_4$:xEu^{3+} phosphors. (b) CIE chromaticity coordinates of $SrWO_4$:20%Eu^{3+}, where the inset shows a digital photograph of $SrWO_4$:20%-Eu^{3+} under near-UV excitation.

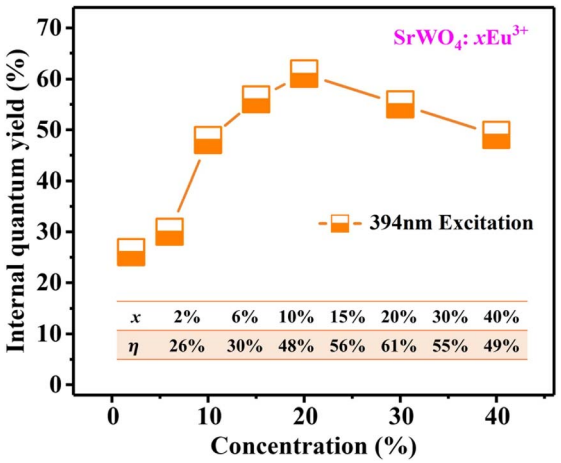

Fig. 6 Internal QY of $SrWO_4$:xEu^{3+} phosphors.

Fluorescence dynamics is a forceful means to investigate the microscopic population process of rare-earth activators. The comprehensive decay times of $SrWO_4$:xEu^{3+} have been measured and calculated through the following first-order exponential equation:[33]

$$I(t) = A\exp(-t/\tau) \quad (1)$$

where $I(t)$ represents the emission intensities at moment t, A is a constant, and τ is the lifetime. In order to better understand the cross-energy transfer (CET) process, the decay curves on $^5D_0$–$^7F_2$ (612 nm) and $^5D_1$–$^7F_1$ (535 nm) of $SrWO_4$:xEu^{3+} phosphors under 394 nm excitation are displayed in Fig. 7a and b. All the experimental data are well matched with the first-order exponential equation (Fig. S11†). The reciprocals of the lifetimes of Eu^{3+} are calculated and fitted (Fig. 7c and d). Evidently, the reciprocals of fluorescence lifetimes on 535 and 612 nm show a nearly linear increase as the Eu^{3+} concentration increases. The experimental data can be fitted with the following function:[44]

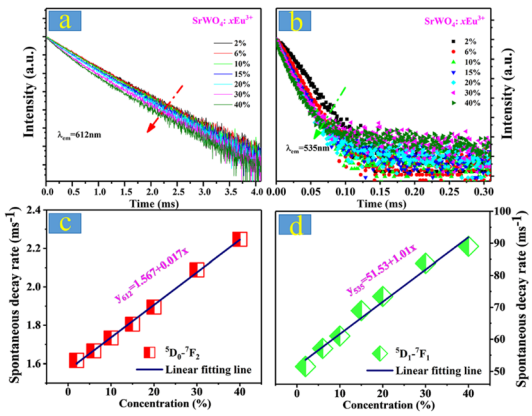

Fig. 7 PL decay curves of (a) $^5D_0$–$^7F_2$ transition (λ_{em} = 612 nm) and (b) $^5D_0$–$^7F_1$ transition (λ_{em} = 535 nm) in $SrWO_4$:xEu^{3+} samples. The changed reciprocal of the fluorescence lifetime of (c) $^5D_0$–$^7F_2$ and (d) $^5D_0$–$^7F_1$ with different Eu^{3+} concentrations.

$$\tau^{-1} \propto R_c + R_{ET}[Eu^{3+}] \quad (2)$$

where R_c represents the total electronic transition rate of Eu^{3+}, which includes the radiative and non-radiative transitions; R_{ET} represents the average CET rate among Eu^{3+} ions; and [Eu^{3+}] represents the Eu^{3+} concentration. Through data fitting, R_c is deduced to be 1.567 and 51.53 ms^{-1} and R_{ET} is deduced to be 0.017 and 1.01 ms^{-1}. This result indicates that the CET rate of Eu^{3+} on $^5D_1$–$^7F_1$ is more serious than on $^5D_0$–$^7F_2$, which can be attributed to the small energy gap of $^5D_1$–$^5D_0$ and large phonon energy of 921 cm^{-1} in the $SrWO_4$ host material (Fig. S8†). In addition, the decay time constant of $Eu_2W_2O_9$ on $^5D_0$–$^7F_2$ transition is measured (Fig. S12†) and the spontaneous emission rate is calculated to be 3.26 ms^{-1}, which is 1.83 times larger than the $SrWO_4$:20%Eu^{3+} sample. Considering the large energy-level spacing of $^5D_0$–$^7F_2$ (16 268 cm^{-1}, about 18 times that of the phonon energy of the $SrWO_4$ host), it can be inferred that the longer fluorescence lifetime in $Eu_2W_2O_9$ on $^5D_0$–$^7F_2$ transition is mainly due to its larger non-radiative transition rate, which derives from the inherent smaller Eu^{3+}–Eu^{3+} ion spacing.

Temperature-dependent emission spectra and dynamics

It is well known that the emission intensities of phosphors strongly depend on the environmental temperature, which is called the thermal-quenching effect. To reveal the thermal-quenching property, the emission spectra of $SrWO_4$:20%Eu^{3+} with a varying temperature range of 300–500 K are displayed in Fig. 8. Evidently, the locations of the emission peaks did not show any change, which is the merit for achieving stable emitting color in the high-temperature range (Fig. S13†). Nevertheless, the emission intensities gradually decrease due to the harmful thermal-quenching effect in the material. Meanwhile, the emission intensity of $SrWO_4$:20%Eu^{3+} can be maintained at 96%, 84%, 68%, and 56% when the temperature is 325, 350, 375, and 400 K, respectively. This indicates that the phosphor has relatively better thermal stability for potential applications in warm WLEDs.[45–48] In order to further reveal the temperature-quenching mechanism of the emission intensity, the temperature-dependent dynamics of $^5D_1$–$^7F_1$ (535 nm) and

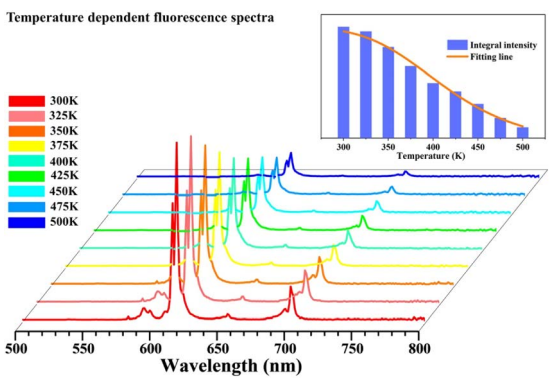

Fig. 8 Temperature-dependent PL intensity of $SrWO_4$:20%Eu^{3+} ranging from 300 to 500 K; the inset shows a fitting function on the related intensity.

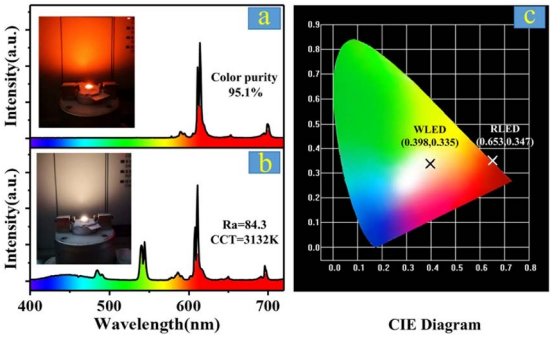

Fig. 9 (a) PL spectra of the $SrWO_4$:20%Eu^{3+} phosphors under near-UV excitation; the inset shows a working red LED. (b) PL spectra of the white light based on the combination of $SrWO_4$:20%Eu^{3+}, YGAB:Tb^{3+}, and BAM:Eu^{2+} phosphors under near-UV excitation, where the inset shows the working WLED. (c) Corresponding chromaticity coordinates in the CIE diagram.

$^5D_0$–$^7F_2$ (612 nm) transitions in $SrWO_4$:20%Eu^{3+} phosphor are also measured (Fig. S14†). The fluorescence lifetimes of 535 and 612 nm are gradually shorter with an increasing temperature, illustrating the important impact on the spontaneous radiation process. Generally, the environmental temperature is an important factor to activate the non-radiative path by raising the phonon vibrational modes and creating an unfavorable condition for photoluminescence.

Applications in red and warm WLEDs

The concentration control of doped Eu^{3+} emitting ions and the increase in efficiency is of critical importance for practical applications. A red-emitting LED device is encapsulated by combining an InGaN near-UV chip (~377 nm) and the $SrWO_4$:20%Eu^{3+} phosphor (Fig. 9a). Clearly, the device emits a bright and pure red emission that can be seen with the naked eye (Fig. 9a, inset), which certifies that the as-prepared $SrWO_4$:Eu^{3+} sample has a satisfactory absorption efficiency and a potential application for warm WLEDs. To further verify the application of quality indoor illumination, a WLED is fabricated by coating the commercial BAM:Eu^{2+} blue-emitting phosphors, YGAB:Tb^{3+} green-emitting phosphors, and the as-prepared $SrWO_4$:20%Eu^{3+} onto a near-UV chip (Fig. 9b). As expected, the combined WLED shows a bright white light with a marginal amount of yellow (Fig. 9b, inset). The as-fabricated WLED displays an effective lighting performance with the CIE chromaticity coordinates of (0.398, 0.335) (Fig. 9c), correlated color temperature (CCT) of 3132 K, and color rendering index (CRI) of 84.3. These experimental results indicate that the facilely prepared non-equivalent substituted $SrWO_4$:xEu^{3+} phosphors have potential application prospects for warm WLEDs.

Conclusions

In summary, a series of highly efficient non-equivalent substituted $SrWO_4$:xEu^{3+} phosphors are successfully synthesized by a simple and facile sol–gel method. The crystal structure, elemental distribution, and PL properties of the as-prepared samples are investigated in detail *via* XRD, EDS, HR-TEM, PL spectra, and fluorescence decay curves. It should be first highlighted that a distinct second-phase $Eu_2W_2O_9$ can be observed in the $SrWO_4$:xEu^{3+} phosphors as the Eu^{3+} concentration is over 20%, accompanied with a decrease in the emission intensity, which represents a potential fluorescence-quenching mechanism by an additional path of phase separation in non-equivalent substituted luminescence materials. It is also discovered that the as-prepared $SrWO_4$:xEu^{3+} phosphors exhibit excellent absorption characteristics in the near-UV spectrum range of 355–425 nm and emit bright red light with the CIE coordinates of (0.653, 0.347) and a highly stable color purity of 94.52%. Finally, the fabricated device displays an effective warm white-light performance with the appropriate CIE coordinates of (0.398, 0.335), low CCT of 3132 K, and favorable CRI of 84.3. In brief, the experimental results show a fresh perspective to view the fluorescence-quenching mechanism of non-equivalent substituted inorganic luminescent materials in warm WLED applications and will provide more opportunities for developing novel efficient luminescent materials.

Conflicts of interest

There are no conflicts to declare.

Acknowledgements

This work was financially supported by grants from the National Natural Science Foundation of China (No. 52102194 and 51902355), Guangdong Basic and Applied Basic Research Foundation (No. 2021A1515010449), Key Research Projects of Colleges and Universities in Henan Province (No. 21A430027).

Notes and references

1 Y. J. Zhang, Z. L. Zhang, X. D. Liu, G. Z. Shao, L. L. Shen, J. M. Liu, W. D. Xiang and X. J. Liang, *Chem. Eng. J.*, 2020, **401**, 125983.
2 Y. Y. Zhou, H. Ming, S. Zhang, T. T. Deng, E. H. Song and Q. Y. Zhang, *Chem. Eng. J.*, 2021, **415**, 128974.
3 D. Zhang, B. F. Zheng, Z. B. Zheng, L. Li, Q. Yang, Y. H. Song, B. Zou and H. F. Zou, *Chem. Eng. J.*, 2022, **431**, 133805.
4 Y. Wei, Z. Y. Cheng and J. Lin, *Chem. Soc. Rev.*, 2019, **48**, 310–350.
5 X. Y. Huang, J. Liang, B. Li, L. L. Sun and J. Lin, *Opt. Lett.*, 2018, **43**, 3305–3308.
6 C. Chen, Y. J. Wu, L. Liu, Y. B. Gao, X. F. Chen, W. B. Bi, X. Liu, D. L. Chen, Q. L. Dai and H. W. Song, *Adv. Sci.*, 2019, **6**, 1802046.
7 A. Forbes, A. Dudley and M. McLaren, *Adv. Opt. Photonics*, 2016, **8**, 200–227.
8 N. Jallouli, L. M. Pastrana-Martinez, A. R. Ribeiro, N. F. F. Moreira, J. L. Faria, O. Hentati, A. M. T. Silva and M. Ksibi, *Chem. Eng. J.*, 2018, **334**, 976–984.

9 H. Rabie, Y. Zhang, N. Pasquale, M. J. Lagos, P. E. Batson and K. B. Lee, *Adv. Mater.*, 2019, **31**, 1970104.
10 H. M. Zhu, C. C. Lin, W. Q. Luo, S. T. Shu, Z. G. Liu, Y. S. Liu, J. T. Kong, E. Ma, Y. G. Cao, R. S. Liu and X. Y. Chen, *Nat. Commun.*, 2014, **5**, 4312.
11 R. Zhang, H. Lin, Y. L. Yu, D. Q. Chen, J. Xu and Y. S. Wang, *Laser Photonics Rev.*, 2014, **8**, 158–164.
12 R. S. Meltzer, S. P. Feofilov, B. Tissue and H. B. Yuan, *Phys. Rev. B*, 1999, **60**, 14012–14015.
13 M. Yu, J. Lin, Z. Wang, J. Fu, S. Wang, H. J. Zhang and Y. C. Han, *Chem. Mater.*, 2002, **14**, 2224–2231.
14 C. D. S. Brites, X. J. Xie, M. L. Debasu, X. Qin, R. F. Chen, W. Huang, J. Rocha, X. G. Liu and L. D. Carlos, *Nat. Nanotechnol.*, 2016, **11**, 851–856.
15 F. W. Kang, Y. Zhang and M. Y. Peng, *Inorg. Chem.*, 2015, **54**, 1462–1473.
16 K. S. Sohn, E. S. Park, C. H. Kim and H. D. Park, *J. Electrochem. Soc.*, 2000, **147**, 4368–4373.
17 C. J. Duan, A. C. A. Delsing and H. T. Hintzen, *Chem. Mater.*, 2009, **21**, 1010–1016.
18 G. Blasse, *Recl. Trav. Chim. Pays-Bas*, 1986, **105**, 143–149.
19 E. Song, J. Wang, J. Shi, T. Deng and Q. Zhang, *ACS Appl. Mater. Interfaces*, 2017, **9**, 8805–8812.
20 H. Ming, S. Liu, L. Liu, J. Peng, J. Fu, F. Du and X. Ye, *ACS Appl. Mater. Interfaces*, 2018, **10**, 19783–19795.
21 L. M. Chen, Y. N. Liu and Y. D. Li, *J. Alloys Compd.*, 2004, **381**, 266–271.
22 M. G. Brik, I. Sildos and V. Kiisk, *Phys. B*, 2010, **405**, 2450–2456.
23 Z. M. El-Bahy, A. A. Ismail and R. M. Mohamed, *J. Hazard. Mater.*, 2009, **166**, 138–143.
24 L. Dacanin, S. R. Lukic, D. M. Petrovic, M. Nikolic and M. D. Dramicanin, *Phys. B*, 2011, **406**, 2319–2322.
25 Y. Jin, J. H. Zhang, S. Z. Lu, H. F. Zhao, X. Zhang and X. J. Wang, *J. Phys. Chem. C*, 2008, **112**, 5860–5864.
26 Z. Xia, G. Liu, J. Wen, Z. Mei, M. Balasubramanian, M. S. Molokeev, L. Peng, L. Gu, D. J. Miller, Q. Liu and K. R. Poeppelmeier, *J. Am. Chem. Soc.*, 2016, **138**, 1158–1161.
27 G. Tian, Z. J. Gu, L. J. Zhou, W. Y. Yin, X. X. Liu, L. Yan, S. Jin, W. L. Ren, G. M. Xing, S. J. Li and Y. L. Zhao, *Adv. Mater.*, 2012, **24**, 1226–1231.
28 S. K. Gupta, P. S. Ghosh, A. K. Yadav, N. Pathak, A. Arya, S. N. Jha, D. Bhattacharyya and R. M. Kadam, *Inorg. Chem.*, 2016, **55**, 1728–1740.
29 K. Li, M. Shang, H. Lian and J. Lin, *Inorg. Chem.*, 2015, **54**, 7992–8002.
30 S. K. Gupta, K. Sudarshan, A. K. Yadav, R. Gupta, D. Bhattacharyya, S. N. Jha and R. M. Kadam, *Inorg. Chem.*, 2018, **57**, 821–832.
31 Y. Wei, J. S. Gao, G. C. Xing, G. G. Li, P. P. Dang, S. S. Liang, Y. S. Huang, C. C. Lin, T. S. Chan and J. Lin, *Inorg. Chem.*, 2019, **58**, 6376–6387.
32 L. Cheng, W. T. Zhang, Y. H. Li, S. Y. Dai, X. F. Chen and K. H. Qiu, *Ceram. Int.*, 2017, **43**, 11244–11249.
33 Maheshwary, B. P. Singh, J. Singh and R. A. Singh, *RSC Adv.*, 2014, **4**, 32605–32621.
34 F. A. Rabuffetti, S. P. Culver, J. S. Lee and R. L. Brutchey, *Nanoscale*, 2014, **6**, 2909–2914.
35 Y. G. Su, L. P. Li and G. S. Li, *Chem. Mater.*, 2008, **20**, 6060–6067.
36 Y. A. Zulueta, T. C. Lim and J. A. Dawson, *J. Phys. Chem. C*, 2017, **121**, 23642–23648.
37 J. A. Dawson, H. Chen and I. Tanaka, *J. Phys. Chem. C*, 2014, **118**, 14485–14494.
38 L. W. W. Fang, R. Zhao, M. Li, K. G. Lim, L. Shi, T. C. Chong and Y. C. Yeo, *J. Appl. Phys.*, 2010, **107**, 104506.
39 S. R. Bathe and P. S. Patil, *Solid State Ionics*, 2008, **179**, 314–323.
40 R. D. Shannon, *Acta Crystallogr., Sect. A: Cryst. Phys., Diffr., Theor. Gen. Crystallogr.*, 1976, **A32**, 751–767.
41 P. F. S. Pereira, A. P. de Moura, I. C. Nogueira, M. V. S. Lima, E. Longo, P. C. de Sousa Filho, O. A. Serra, E. J. Nassar and I. L. V. Rosa, *J. Alloys Compd.*, 2012, **526**, 11–21.
42 J. Li, J. Yan, D. Wen, W. U. Khan, J. Shi, M. Wu and Q. Su, *J. Mater. Chem. C*, 2016, **4**, 8611–8623.
43 H. Guo, X. Huang and Y. Zeng, *J. Alloys Compd.*, 2018, **741**, 300–306.
44 Y. Wang, W. Xu, S. Cui, S. Xu, Z. Yin, H. Song, P. Zhou, X. Liu, L. Xu and H. Cui, *Nanoscale*, 2015, **7**, 1363–1373.
45 P. Du, X. Huang and J. S. Yu, *Chem. Eng. J.*, 2018, **337**, 91–100.
46 X. Huang, B. Li and H. Guo, *Ceram. Int.*, 2017, **43**, 10566–10571.
47 H. Deng, Z. Gao, N. Xue, J. H. Jeong and R. Yu, *J. Lumin.*, 2017, **192**, 684–689.
48 J. Li, Q. Liang, Y. Cao, J. Yan, J. Zhou, Y. Xu, L. Dolgov, Y. Meng, J. Shi and M. Wu, *ACS Appl. Mater. Interfaces*, 2018, **10**, 41479–41486.